American Mineralogist, Volume 110, pages 570–581, 2025

Synthesis and characterization of Fe-poor olivine with applications to the surface of Mercury

Brendan A. Anzures[1,*,**], **Kathleen E. Vander Kaaden**[1,2,†], **Francis M. McCubbin**[3,‡], **Richard L. Rowland II**[1,4,†], **Gordon M. Moore**[1,4,†], **Kelsey Prissel**[1,§], **Richard V. Morris**[3], **Rachel L. Klima**[5,||], **Karen R. Stockstill-Cahill**[5], and **David G. Agresti**[6]

[1]Jacobs, NASA Johnson Space Center, 2101 NASA Parkway, Houston, Texas 77058, U.S.A.
[2]NASA Headquarters, Mary W. Jackson Building, Washington, D.C. 20546, U.S.A.
[3]ARES NASA Johnson Space Center, 2101 NASA Parkway, Houston, Texas 77058, U.S.A.
[4]Los Alamos National Laboratory, Los Alamos, New Mexico 87545, U.S.A.
[5]The Johns Hopkins University Applied Physics Laboratory, 11100 Johns Hopkins Road, Laurel, Maryland 20723, U.S.A.
[6]Department of Physics, University of Alabama at Birmingham, 902 14th Street South, Birmingham, Alabama 35294, U.S.A.

Abstract

Results from X-ray remote sensing aboard NASA's MErcury Surface Space ENvironment GEochemistry and Ranging (MESSENGER) spacecraft have demonstrated that Mercury has a low, but measurable, concentration of Fe on its surface. However, ultraviolet to near-infrared spectroscopic measurements of the mercurian surface do not show the 1 μm absorption band characteristic of ferromagnesian silicates. This observation is consistent across multiple Fe-bearing terranes with a range of ages, suggesting the Fe present on Mercury's surface may not be stored within silicate phases. To further constrain the possible mineralogy and composition of Fe-bearing phases on Mercury, we used various spectroscopic techniques to characterize synthetic olivine with minor amounts of Fe (i.e., $Fo_{99.62}$–$Fo_{99.99}$) and more Fe-rich natural olivines. Our results indicate that the distinctive 1 μm absorption band of olivine is detectable in reflectance spectra of olivine at a concentration as low as 0.03 wt% FeO and 0.01 wt% in continuum removed data. Additionally, MESSENGER's lack of a 1 μm absorption, taking into account Mercury Dual Imaging System (MDIS)'s limited spectral resolution and Mercury Atmospheric and Surface Composition Spectrometer (MASCS)'s high signal-to-noise ratio, suggests there is <0.38 wt%, and likely <0.01 wt%, FeO on the surface of Mercury. Because the 1 μm band is not observed in surface spectra, these results indicate that the Fe observed on the surface of Mercury is not bound in an olivine structure. Rather, we posit that Fe is present as nano-phase and macroscopic Fe-rich metal or Fe-sulfide that formed as a result of space weathering and igneous smelting processes. Looking forward to ESA/JAXA's BepiColombo mission that has a planned Mercury orbit arrival time in December 2025, Mercury Radiometer and Thermal Infrared Imaging Spectrometer (MERTIS) mid-infrared spectra should provide a mineralogical detection or absence of olivine where MIR spectral features are still present even in synthetic olivines with minor amounts of Fe ($Fo_{99.99}$).

Keywords: Mercury, olivine, reflectance spectroscopy, space weathering

Introduction

Ferromagnesian silicates like olivine are dominant minerals in planetary mantles and on planetary surfaces. Their early crystallization in mafic-ultramafic magmatic systems makes them an important tool for understanding the thermal and magmatic history of rocky planetary bodies in our solar system (e.g., Day et al. 2019; Filiberto and Dasgupta 2011; Karner et al. 2003; Longhi et al. 2010; Papike et al. 2003; Roeder and Emslie 1970; Shearer et al. 2008; Singletary and Grove 2006; Toplis 2005). Furthermore, reflectance spectra of ferromagnesian silicates display a diagnostic absorption feature near 1 μm wavelength caused by crystal field transitions of Fe^{2+} in octahedral sites of the crystal structure. This 1 μm absorption can be observed in the reflectance spectroscopy of planetary surfaces acquired by orbiting spacecraft (e.g., Burns 1993). The reader is referred to Dyar et al. (2009), Isaacson et al. (2014), and Sunshine and Pieters (1998) for a more complete discussion on the olivine structure and its effect on the interpretation of spectroscopic analyses. Unlike Fe-rich olivine, the pure Mg end-member (i.e., forsterite) does not display a 1 μm absorption feature due to the absence of Fe^{2+}, but its spectral strength changes rapidly and nonlinearly with increasing FeO and decreasing Mg# (e.g., band depth vs. X_{FeO}) (Klima et al. 2007). However, little is known about the minimum amount of FeO needed in olivine before the 1 μm absorption band is detected. This information is necessary to interpret spectra from low-FeO planetary surfaces such as Mercury and many E-type asteroids.

The 1 μm absorption feature associated with ferromagnesian silicates is nearly ubiquitous in the reflectance spectra of planetary bodies across the Solar System. Yet, this spectral feature has not been observed for Mercury despite the presence of ~1–2 wt%

---

* Corresponding author E-mail: brendan.a.anzures@nasa.gov. Orcid https://orcid.org/0000-0002-5549-1631

† The second affiliation listed is the author's present address.

‡ Orcid https://orcid.org/0000-0002-2101-4431

§ Orcid https://orcid.org/0000-0002-0129-2215

|| Orcid https://orcid.org/0000-0002-9151-6429

0003-004X/25/0004–570$05.00/DOI: https://doi.org/10.2138/am-2024-9400

levels of Fe detected on the surface by X-ray spectroscopy (Holsclaw et al. 2010; Izenberg et al. 2014; Murchie et al. 2015; Nittler et al. 2011; Weider et al. 2014). Consequently, obtaining a quantitative understanding of the detection limit for a 1 μm absorption feature as a function of FeO content in ferromagnesian silicate minerals could substantially improve our knowledge of Mercury and the nature of Fe at its surface.

One of the primary reasons we do not have quantitative constraints on the amount of FeO required to produce a 1 μm absorption feature in olivine is the lack of pure, well-crystallized, and well-characterized synthetic materials of appropriate composition. Suites of synthetic minerals have proven very valuable for exploring spectral systematics of pure quadrilateral pyroxenes (Klima et al. 2007, 2011), the Mg-Fe olivine series (Dyar et al. 2009; Isaacson et al. 2014), and iron-bearing oxides (Jackson et al. 2014; Williams et al. 2016). These studies highlight the importance of using multiple analytical techniques to characterize synthetic samples well (particularly those that are low in iron and not dominated by strong absorption bands) before using them as spectral calibration standards. Because crystal field spectra are sensitive to cation oxidation state (e.g., Fe^{2+} and Fe^{3+}), trace amounts of either cation incorporated into a mineral's structure can drastically alter the visible-near-infrared spectrum. Here we synthesize forsteritic olivine with 0.01 wt% FeO to 0.39 wt% FeO, as well as synthetic fayalite to fully characterize the effect of Fe^{2+} on 1 μm absorption bands using various analytical techniques including powdered X-ray diffraction (XRD), scanning electron microscopy (SEM), electron probe microanalysis (EPMA), Mössbauer spectroscopy, as well as ultraviolet (UV), visible (VIS), and infrared (IR) spectroscopy.

METHODS

Starting materials

Olivine starting materials consisted of a combination of reagent-grade oxides (e.g., MgO, SiO_2, Fe_2O_3), reagent-grade talc (magnesium silicate monohydrate), natural talc (with minor FeO), or handpicked San Carlos olivine crystals (SC-001; Table 1). Forsterite starting mixtures were produced by mixing MgO with SiO_2 (F-S sample labels) or talc (F-T sample labels) such that the Si:Mg ratio matched the stoichiometry of forsterite. A fayalite starting mixture was produced by weighing out the respective amounts of SiO_2 and Fe_2O_3 reagent-grade oxides such that the Si:Fe ratio matched the stoichiometry of fayalite. After weighing, each starting material was mixed under ethanol in either an Fe-free Retsch ball mill with ZrO_2 cups and ZrO_2 balls (for forsterite mixes), a Fritsch Pulverisette automated mixer, or by hand in a mortar and pestle for 30 min to 2 h.

Experimental methods

Most of the forsteritic olivine syntheses were conducted by loading the powdered oxide mixtures into a $Pt_{95}Au_5$ crucible before heating at 1600 °C for 8–12 h in a Lindberg box oven at NASA's Johnson Space Center (JSC). The forsteritic F-S-003 sample was synthesized by loading the powdered oxide mixture into a FeO-free Al_2O_3 crucible before heating at 1500 °C for 8–12 h with a 5 h ramp up to temperature. The experiments were terminated by shutting off the power to the furnace and leaving the sample in the furnace to cool. Once cool to the touch, the crucible was removed from the furnace, and the sample was reground in a mortar and pestle. This process was repeated at least twice for all samples, with the total run time for each sample given in Table 1.

The fayalite sample (CF002) was produced in a DelTech tube furnace following procedures outlined in Vander Kaaden et al. (2015). The synthesis of fayalite CF002 was conducted by placing an Fe-soaked Pt crucible with the starting material in a DelTech 1-atmosphere gas-mixing (CO-CO_2) furnace at 1100 °C for 24 h at an oxygen fugacity of IW+1 controlled by CO-CO_2 gas mixing. This process was repeated three times, with the sample recovered and ground to a powder in between each heating step and the total run time given in Table 1.

Initial characterization of the forsteritic samples by EPMA (Table 2) detected 0.01 to 0.53 wt% total FeO contamination. In particular, the two syntheses that used talc as a starting material (F-T-002 and F-T-004) had the highest total Fe concentrations (0.39 and 0.53 wt% FeO_T, respectively where FeO_T indicates total Fe reported as FeO, regardless of the oxidation state of Fe), which facilitated our investigation of olivine with FeO abundances intermediate between 0.53 wt% FeO and end-member forsterite. To investigate the effects of a finer range of Fe composition on the spectroscopic properties of forsteritic olivine, F-S-002 was mixed in two different proportions with the nominally pure forsterite F-S-003. These two resulting blends (F-S-006 and F-S-007) were subsequently ground, placed in an Al_2O_3 crucible, and homogenized for 72 h in a Deltech gas-mixing furnace at 1300 °C with an oxygen fugacity of IW+1. The San Carlos reference material SC-001 was similarly treated in the Deltech to ensure that nearly all Fe was present as ferrous iron. A summary of the run conditions for all experiments is provided in Table 1.

Powdered X-ray diffraction (XRD)

Synthetic olivine purity was assessed by powder X-ray diffraction in a PANalytical X'PERT Pro MPD diffractometer fitted with a cobalt X-ray source ($CoK\alpha_1$ $\lambda = 1.79801$ Å) and an X'celerator (2.02° 2θ) detector at NASA JSC. After experimental heating and synthesis, an aliquot of each sample was grounded by hand in a mortar and pestle. The XRD patterns were collected in angular dispersive mode from 4.0224 to 79.9784 °2θ with a step size of 0.0170° for 20.32 s per step on a traditional spinner stage. Data analysis was completed using X'Pert High Score Plus software, comparing the patterns to standards ICDD #98-004-7150 forsterite, #98-000-5628 fayalite, or #01-073-9573 Fe_2SiO_4 iron silicate.

TABLE 1. Experimental conditions

Sample	T (°C)	Duration (h)	Mix Proportions (wt%)	fO_2 (ΔIW)	Crucible
F-S-003	1500	16–24	42.70:57.30 SiO_2:MgO[a]	ambient	Fe-free Al_2O_3
F-S-007	1300	72	10:90 F-S-002:F-S-003	IW+1	Fe-free Al_2O_3
F-S-006	1300	72	50:50 F-S-002:F-S-003	IW+1	Fe-free Al_2O_3
F-S-002	1600	≥16	42.75:57.25 SiO_2:MgO[a]	ambient	$Pt_{95}Au_5$
F-T-004	1600	≥16	34.69:65.31 MgO:Alfa Aesar Talc[b]	ambient	$Pt_{95}Au_5$
F-T-002	1600	≥16	34.74:65.26 MgO:Natural Talc[c]	ambient	$Pt_{95}Au_5$
SC-001	1300	72	Natural San Carlos Olivine	IW+1	Fe-saturated Pt
CF002	1100	72	27.34:72.66 SiO_2:Fe_2O_3	IW+1	Fe-saturated Pt

[a] Fe contamination from EM Science MgO (≥0.01 wt% FeO).
[b] Fe contamination from Alfa Aesar Talc (≥0.25 wt% FeO).
[c] Fe contamination from Natural Talc (≥0.20 wt% FeO).

Table 2. Average major and minor element compositions (wt%) of synthetic olivine from EPMA

wt%	F-S-003	F-S-007	F-S-006	F-S-002	F-T-004[a]	F-T-002	SC001	CF002
SiO_2	42.20 (16)	41.59 (29)	41.80 (35)	42.26 (13)	41.42 (22)	42.07 (39)	40.32 (15)	29.27 (35)
Al_2O_3	0.25 (22)	0.21 (27)	0.21 (1)	b.d.	0.51 (10)	0.07 (4)	0.01 (2)	0.05 (6)
FeO	0.01 (0)	0.01 (0)	0.03 (1)	0.05 (2)	0.37 (1)	0.39 (5)	9.01 (49)	69.99 (36)
Fe_2O_3	–	–	–	–	0.20 (1)	–	–	–
MgO	58.03 (35)	58.01 (30)	58.69 (39)	58.45 (27)	57.88 (41)	57.74 (48)	50.54 (56)	0.01 (1)
CaO	0.01 (1)	0.02 (0)	0.02 (1)	0.01 (0)	0.12 (5)	0.01 (0)	0.08 (1)	0.02 (1)
Total	100.50 (44)	99.84 (50)	100.54 (52)	100.77 (30)	100.49 (48)	100.29 (62)	99.96 (76)	99.34 (51)
Mg#	99.99	99.99	99.97	99.95	99.64	99.62	90.91	0.03
N	41	12	34	51	36	35	50	44

Notes: *N* = number of analyses. b.d. = abundance was below detection limit. "–" = value not computed. All parenthetical values represent 1-sigma standard deviation of the mean.

[a] Mössbauer data of F-T-004 used to compute Fe^{3+} vs. Fe^{2+}.

Scanning electron microscope (SEM) analysis

The grain size and shape of synthetic powders were measured using the JEOL 7600F field emission scanning electron microscope at NASA JSC. Aliquots of each sample were scooped onto an aluminum metal SEM stub covered with double-sided carbon tape. Each SEM stub was then carbon coated to a thickness of ~32 nm to avoid charging effects. Approximately 10 high-resolution secondary electron images were taken of each sample using an accelerating voltage of 15 keV, and representative images are shown in Figure 1. To characterize the grain size of each sample, the long and short dimensions were measured ~20 grains in each image for a total of 160–230 grains per sample (Table 3).

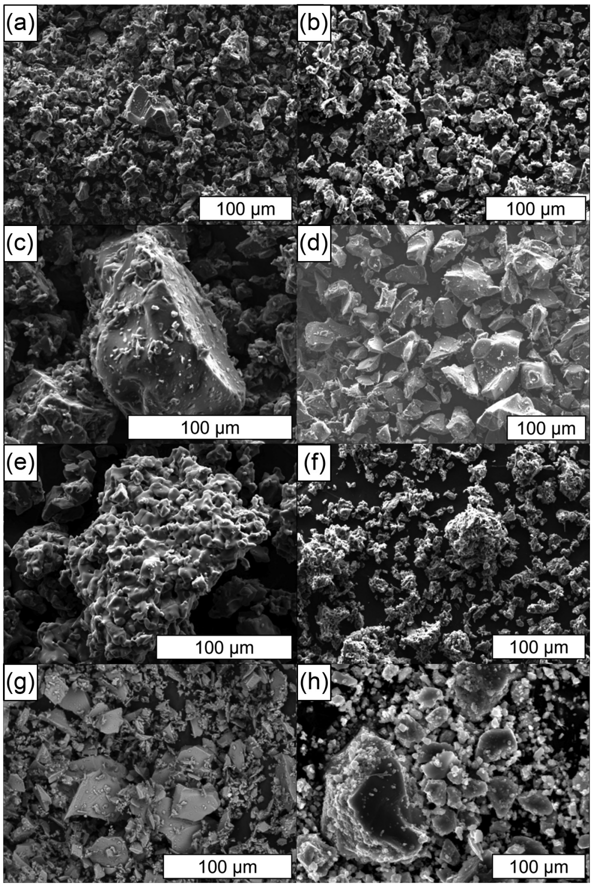

Figure 1. High-resolution secondary electron images of synthesized olivine powders ordered by increasing Fe content used for grain analysis: (**a**) F-S-003; (**b**) F-S-007; (**c**) F-S-006; (**d**) F-S-002; (**e**) F-T-004; (**f**) F-T-002; (**g**) SC-001; (**h**) CF002.

Electron probe microanalysis (EPMA)

Quantitative major and minor element compositions were measured by EPMA using the JEOL 8530 field emission microprobe at NASA JSC. Aliquots from each sample were embedded in epoxy, polished down to a 0.3 μm finish using Al_2O_3 as the polishing substrate, and carbon-coated to a thickness of 20 nm before analysis. All analyses were conducted using an accelerating voltage of 15 keV, a 5 μm spot size, and a beam current of 70 nA to ensure a reasonable detection level for iron. Analytical standards included Springwater olivine (Si, Mg), San Carlos olivine (Fe, Mg), Great Sitkin-Anorthite (Al, Ca), and fayalite (Fe). In particular, we used San Carlos olivine as an Fe standard for low-FeO olivine and fayalite as a standard for synthetic fayalite. Peak count times ranged from 30 to 60 s, and background count times ranged from 15 to 30 s. The detection limit achieved for FeO in our analyses was ~70 ppm.

UV-VIS-IR spectroscopy

Reflectance spectra were acquired on <125 μm dry-sieved powders using a UV-VIS-NIR bidirectional reflectance (BDR) spectrometer (0.3–2.6 μm) and a Thermo Nexus 870 FTIR spectrometer (1.4–50) in the Reflectance Experiment LABoratory (RELAB), a NASA-supported multi-user spectroscopy facility at Brown University. In addition, ultraviolet measurements (0.21–0.4 μm) were collected at the Johns Hopkins Applied Physics Labortaory's Laboratory for Spectroscopy under Planetary Environmental Conditions (LabSPEC) using a Macphersen vacuum UV source and monochrometer with a photomultiplier tube and a ground MgF_2 reference standard. At LabSPEC, samples were mounted behind a MgF_2 window in an UHV (~10^{-9} Torr) chamber. In RELAB, the samples were filled into 9 mm dishes and measured relative to a halon reference standard using the Bidirectional Reflectance spectrometer from 0.3–2.6 μm with an incidence angle of 30° and emission angle of 0° under ambient conditions. Samples were rotated during measurement to provide a more uniform scattering environment (Pieters et al. 1983). Samples were then measured relative to a diffuse gold reference standard in a dry-air-purged environment using a Nicolet Nexus 870 FTIR spectrometer (biconical geometry) over the wavelength range of 1.3–50 μm. The FTIR measurements were scaled and spliced into the absolute reflectance measured by the bidirectional spectrometer at a point between 2.65 and 4.4 μm where the spectra aligned well. UV spectra from LabSPEC were spliced into the RELAB data between 0.3–0.4 μm. In most samples, the overlapping 0.3–0.4 μm regions were consistent between both laboratories and required no scaling. In the other samples (F-S-002, F-T-004, F-T-002), the LabSPEC spectra required a small scaling factor to match the RELAB data. A piecewise convex hull continuum was fit to the spectra between 0.3 and 2.6 μm to produce continuum-removed spectra around the main 1 μm olivine absorption.

Mössbauer spectroscopy

Mössbauer spectra were obtained at NASA JSC in a backscatter measurement geometry, at room temperature, and on powdered samples using spectrometers by ESPI Inc., similar to those employed by the Mars Exploration Rovers (Klingelhöfer et al. 2003) to determine the ferric/ferrous ratio of F-T-004 olivine, which appeared to be oxidized. The measurements were made directly on the powders, preserving 0.5 to 15 g aliquots that remained uncontaminated for later studies. The computer programs MERView and MERFit were used, respectively, to velocity calibrate and least-squares fit the spectra (Agresti et al. 2006; Agresti and Gerakines 2009). Areas and widths of doublet peaks (Lorentzian line shapes) were constrained to be equal during the fitting procedures. The values of the center shift are

Table 3. Synthetic powder grain sizes from SEM analysis

Sample	n	Long Dimension Min (μm)	Long Dimension Max (μm)	Short Dimension Min (μm)	Short Dimension Max (μm)	Mean Average Dimension (μm)	Median Average Dimension (μm)
F-S-003	210	6.3	180.4	4.0	83.4	23.2	17.3
F-S-007	200	4.7	73.4	54.5	54.5	20.4	17.9
F-S0-006	220	4.4	149.6	2.9	101.4	38.3	33.0
F-S-002	161	14.3	166.9	10.0	116.5	57.9	54.7
F-T-004	200	0.8	61.7	0.4	42.2	10.6	7.6
F-T-002	200	1.2	64.3	0.7	43.2	11.7	8.4
CF002	231	0.2	38.9	0.1	36.3	3.1	2.0

reported with respect to metallic Fe foil at room temperature. Subspectral areas include a correction factor (the f-factor) to account for differences in the recoil-free fractions of Fe^{2+} and Fe^{3+} [$f(Fe^{3+})/f(Fe^{2+}) = 1.21$ independent of mineralogical composition]. Mössbauer parameter (center shift, CS; quadrupole splitting, QS; full-width at half maximum intensity, and subspectral area) are based on various independent fits described in more detail by Morris et al. (2006).

Results

Powdered X-ray diffraction patterns

Powdered XRD analyses were conducted to assess the purity of our run products and to determine whether any unreacted starting material remained after synthesis. Each forsterite sample produced a 100% match to the reference forsterite (ICDD #98-004-7150) with the chemical formula Mg_2SiO_4. The fayalite synthesis (CF-002) resulted in a 100% match to the referenced fayalite (01-073-9573) with the chemical formula Fe_2SiO_4. The San Carlos olivine sample that was used as reference material produced a 100% match to the reference ferroan forsterite (#98-004-6152) with the chemical formula $Fe_{0.188}Mg_{1.812}SiO_4$. Additionally, the XRD standard's Mg# of 90.6 is close to the EPMA calculated Mg# of 90.91. Representative powder XRD patterns for a forsterite synthesis (F-S-003), San Carlos olivine (SC-001), and the fayalite synthesis (CF-002) are shown in Figure 2.

Grain size analysis from SEM

Grain sizes of synthetic olivines were relatively small, with median and mean grain sizes ranging from 2.0 and 3.1 μm (CF002) to 54.7 and 57.9 μm (F-S-002), respectively, and summarized in Table 3. Individual grains ranged in size from 0.1–116.5 μm in the shortest direction and 0.2–180.4 μm in the longest direction. All of the synthetic olivine experiments produced right-skewed grain size distributions with the median lower than the mean, as shown in Figure 3 histograms.

Chemical composition of synthetic olivines from EPMA and Mössbauer spectroscopy

All sample powders were analyzed using EPMA; the results are shown in Table 2. The composition of the San Carlos olivine (i.e., Fo_{91}) sample from EPMA is consistent with published values for San Carlos olivine (e.g., Fournelle 2011). The FeO_T abundances of our forsteritic olivine samples range from 0.01–0.53 wt% FeO_T. When sample F-T-004 was extracted from the furnace, it exhibited a noticeable orange tint characteristic of Fe oxidation. The VIS-NIR spectrum (Fig. 5b) of this sample revealed an absorption band at 0.5 μm, indicative of the presence of Fe^{3+} in the sample (e.g., Clark 1999). Mössbauer analyses were then conducted to determine the ratio of Fe^{3+} to total Fe present in the sample. These analyses (Fig. 4) resulted in a Fe^{3+} to total Fe of 0.32 ± 0.02. Combining these results with the EPMA data allows for the calculation of FeO and Fe_2O_3 in sample F-T-004, resulting in 0.37 wt% FeO and 0.20 wt% Fe_2O_3 (Table 2). Because none of the reflectance spectra from other samples exhibited an absorption feature at 0.5 μm, the Fe detected by EPMA is assumed to be Fe^{2+} and reported as FeO. In summary, for the synthetic forsterite samples, MgO

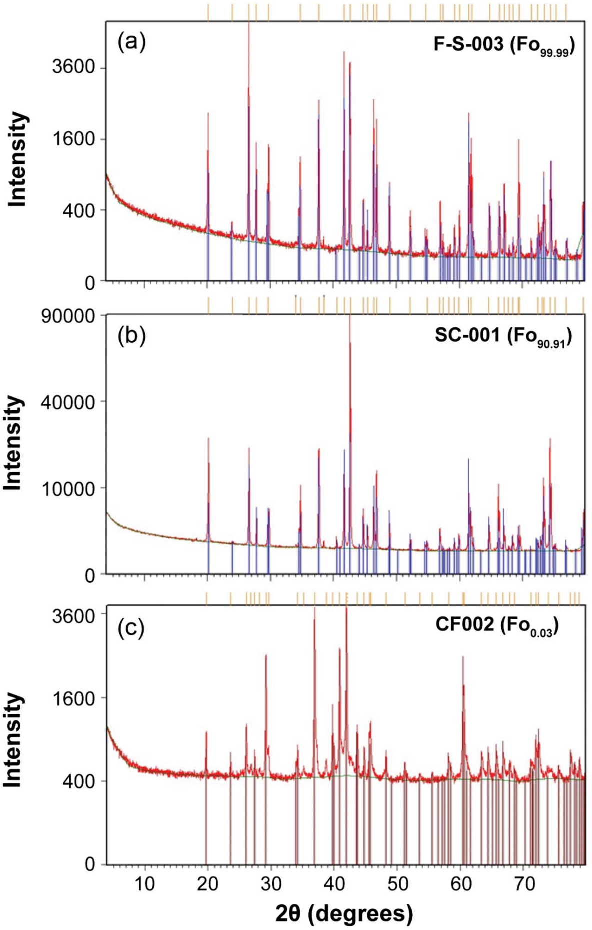

Figure 2. Measured powder XRD patterns of synthesized (**a**) forsterite (F-S-003), (**b**) San Carlos olivine (SC-001), and (**c**) fayalite (CF002). Colored sticks represent the approximate locations of olivine compared standards (**a**) ICDD #98-004-7150 forsterite, (**b**) #98000–5628 fayalite, and (**c**) #01-073-9573 Fe_2SiO_4 iron silicate.

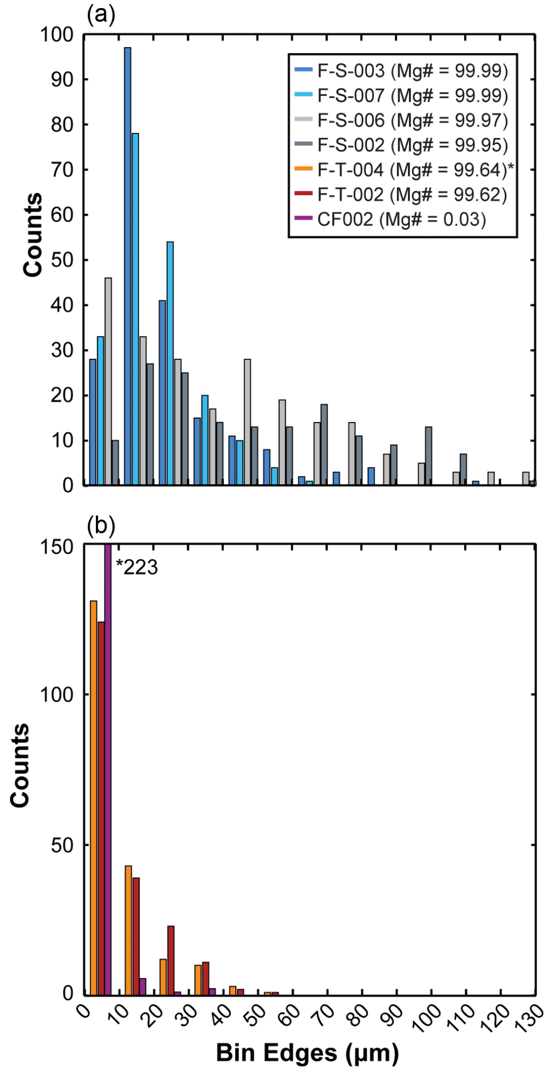

FIGURE 3. Histograms of average grain sizes of synthetic olivines. (**a**) F-S-003, F-S-007, F-S-006, F-S-002. (**b**) F-T-004, F-T-002, CF002 (*223 grains <10 μm in length).

values ranged from 57.74 to 58.69 wt%, and FeO values ranged from 0.01 to 0.39 wt%. These FeO abundances correspond to a range in Mg# [Mg/(Mg+Fe)·100] of 99.62 to 99.99. The fayalite sample contained 0.01 wt% MgO with a calculated Mg# of 0.03.

UV-VIS-IR spectroscopic analyses

Characteristic olivine absorptions in reflectance spectra [UV-VIS-NIR (0.2–2.6 μm) and IR (200–2221 $\text{cm}^{-;1}$)] show a clear relationship with FeO abundance (Figs. 5 and 6). Specifically, the 1 μm olivine absorption varies with FeO (Fig. 5), and select spectral band parameters are shown in Figure 7 and summarized in Table 4. The 1 μm absorption strength systematically decreases with decreasing FeO content and increasing Mg# as seen in bidirectional absolute reflectance (Fig. 5a). The fayalite sample CF-002 had the greatest 1 μm absorption depth due to its high FeO content (~70 wt% FeO and Mg# of 0.03), and San Carlos olivine (~9 wt% FeO and Mg# of 90.91) had the second strongest 1 μm absorption within our measured data set. For samples F-S-003 and F-S-007 (0.01 wt% FeO and Mg# of 99.99), no obvious 1 μm absorption band was seen in absolute reflectance. However, there was an observable 1 μm absorption that increases in strength with increasing FeO in olivine with as little as 0.03 wt% FeO, corresponding to an Mg# of 99.97. Continuum-removed reflectance spectra did tease out extremely weak 1 μm absorptions for even the $\text{Fo}_{99.99}$ olivines with 0.01 wt% FeO (Fig. 5b). As noted in previous studies (e.g., Adams 1975; Burns 1970, 1993; King and Ridley 1987), the band center for fayalite shifted to longer wavelengths (~1.10 μm) compared to the forsteritic samples (~1.06 μm). There was no discernible increase in the 1 μm band center position from the low-Fe synthetic olivines ($\text{Fo}_{99.62–99.99}$) to the San Carlos olivine (Fo_{91}).

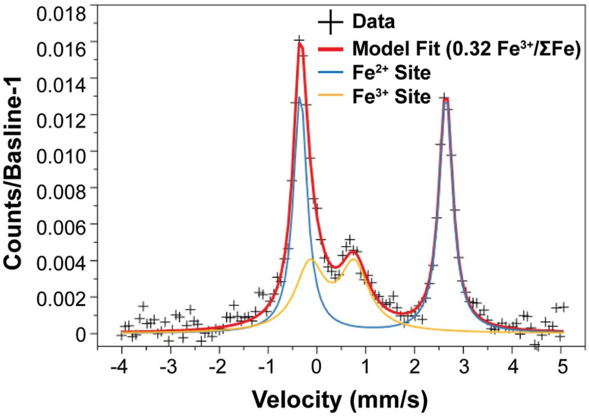

FIGURE 4. Mössbauer data of synthetic olivine F-T-004 indicates the presence of Fe^{3+} due to oxidation of forsteritic olivine. Best model fit results in 0.32 ± 0.02 $\text{Fe}^{3+}/\Sigma\text{Fe}$ (0.37 wt% FeO and 0.20 wt% Fe_2O_3).

Spectral reflectance absorption/emissivity feature changes as a function of olivine FeO abundance were also observed in the IR, subdivided into the intermediate mid-infrared (IMIR) region (4.5–7.0 μm wavelength or 1430–2221 cm^{-1} wavenumber) (Fig. 6a) and MIR (200–1200 cm^{-1} wavenumber) (Fig. 6b), with band parameters summarized in Table 4. Kremer et al. (2020) found that olivine IMIR absorptions, particularly the 5.6 and 6.0 μm bands, shift to shorter wavelengths by 0.11 and 0.10 μm, respectively, across the Mg-Fe olivine solid solution. Here, IMIR absorptions do not appear to systematically vary within $\text{Fo}_{99.62}$-$\text{Fo}_{99.99}$, although a small shift of 2 cm^{-1} is seen in larger Mg# steps from $\text{Fo}_{99.62}$ to $\text{Fo}_{90.91}$. Interestingly, the lower wavelength absorption features at 4.9, 5.2, and 5.4 μm are more prominent in these high-Mg olivines (Mg# >80) compared to flattened features in high-Fe olivine (Mg# <20) (Kremer et al. 2020). Therefore, the IMIR region represents a powerful remote sensing tool to detect the presence of olivine and characterize Mg# even in samples where the 1 μm olivine band is obscured due to low FeO abundance (this study) or where olivine exists as a minor phase in a multi-component sample, or where olivine coexists with nanophase Fe [e.g., lunar pyroclastic soils and martian meteorite NWA 2737 from Kremer et al. (2020)].

The use of MIR to determine olivine Mg# has been previously explored (e.g., Hamilton 2010), though the MIR Christiansen and

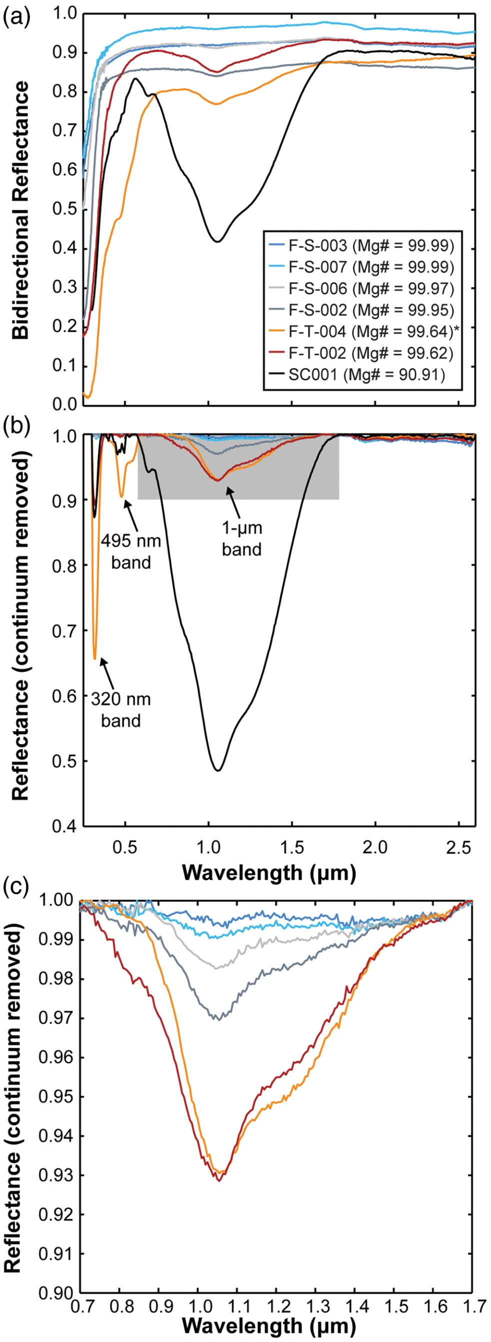

FIGURE 5. UV-VIS-NIR reflectance spectra of synthetic olivine powders sieved to <125 µm grain size with median grain sizes from 7.6–54.7, as summarized in Table 3. Low-FeO olivine and San Carlos olivine (**a**) bidirectional reflectance spectra and (**b**) continuum removed reflectance spectra. (**c**) Emphasis on the 1 µm absorption, including only low-FeO olivine (Fo$_{99.62}$–Fo$_{99.99}$). A detectable 1 µm absorption (the principal olivine absorption near 1 µm caused by Fe^{2+} ions in the M1 and M2 sites) is detectable in olivine with an FeO abundance of as low as 0.03 wt% in bidirectional reflectance and 0.01 wt% in continuum removed reflectance. A 495 nm absorption due to the presence of minor Fe^{3+} in oxidized F-T-004 olivine (Shestopalov and Golubeva 2006).

transparency features (Salisbury 1993) are not well constrained due to their nonunique origin arising from Si-O stretching and bending motions. Here, the first Christansen feature (CF1) was observed to shift systematically to higher wavenumbers with decreasing FeO abundance (Figs. 6b and 7b), presumably due

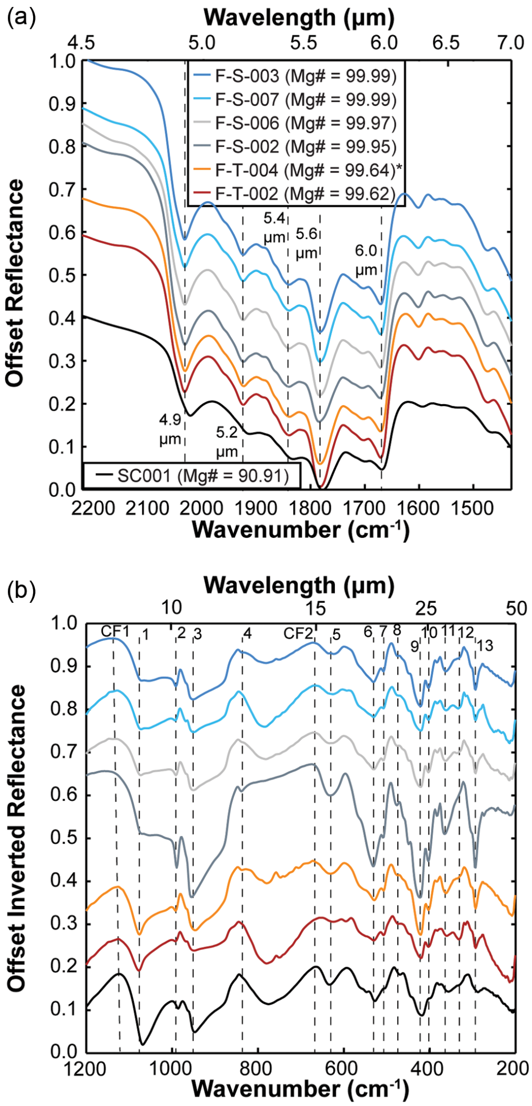

FIGURE 6. Reflectance spectra of synthetic olivine in the (**a**) intermediate mid-infrared (IMIR) infrared region and (**b**) MIR region, where features are the result of (**b**) fundamental molecular vibrations and (**a**) overtone-combinations of these molecular and crystal lattice vibrations. (**a**) IMIR absorptions do not appear to vary systematically within Fo$_{99.62}$–Fo$_{99.99}$, although a shift is seen in larger Mg# steps from Fo$_{99.62}$–Fo$_{99.99}$ to Fo$_{90.91}$. Interestingly, the lower wavelength absorption features at 4.9, 5.2, and 5.4 µm are more prominent in this high-Mg olivine compared to flattened features in high-Fe olivine. (**b**) Reststrahlen bands caused by stretching and bending motions of Si-O are labeled 1–13 and do not appear to systematically vary within Fo$_{99.62}$–Fo$_{99.99}$, although a shift is seen in larger Mg# steps from Fo$_{99.62}$–Fo$_{99.99}$ to Fo$_{90.91}$. (**b**) Christiansen features, the reflectance minimum/emission maximum, may also shift to lower wavenumbers due to increasing polymerization, and a systematic variation is observed in CF1 within Fo$_{99.62}$–Fo$_{99.99}$.

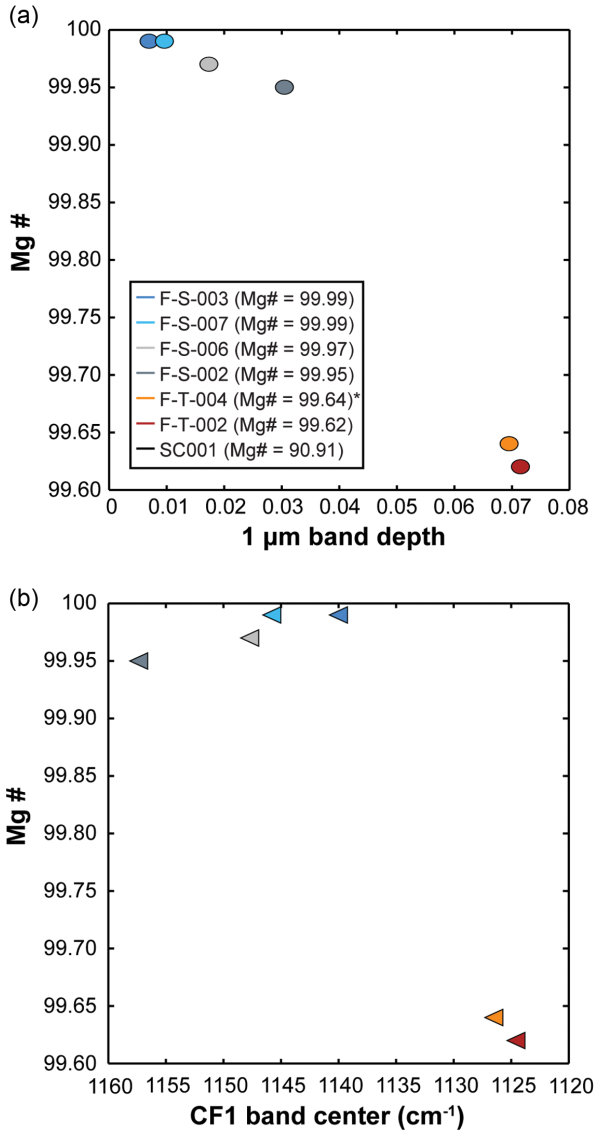

Figure 7. Spectral band parameters shift with Mg# where the (**a**) 1 µm band depth decreases and (**b**) CF1 Christiansen feature band center shifts toward higher wavenumbers with increasing Mg, respectively.

to decreasing polymerization (Hamilton 2010). However, reststrahlen bands caused by stretching and bending motions of Si-O do not appear to vary systematically within the range of $Fo_{99.62}$-$Fo_{99.99}$, although a shift is seen when Mg# decreases to $Fo_{90.91}$. Nevertheless, discernable olivine reflectance/emissivity features are observed in samples where the 1 µm olivine band is extremely weak due to low FeO abundance ($Fo_{99.62–99.99}$), mirroring the IMIR region as a powerful indicator of olivine.

DISCUSSION

Comparison to previous studies

The use of olivine spectral features for compositional analysis has been explored in numerous previous studies (Dyar et al. 2009; Isaacson et al. 2014; Lane et al. 2011; Sunshine and Pieters 1998). Sunshine and Pieters (1998) examined a series of natural olivine samples ranging in composition from Fo_0 to Fo_{97}. Among these results, the intensity of the reflectance spectra absorptions at ~1 µm generally increases with increasing Fe^{2+} in the M2 site of olivine, a trend that continues into the higher Mg#s explored in this study. Given the impurities that exist within natural samples and the effects these impurities can have on reflectance data, Dyar et al. (2009) synthesized a series of olivines from forsterite to fayalite in 5–10 mol% increments. These materials were analyzed using various techniques in three studies to provide a comprehensive understanding of olivine spectroscopic properties across the forsterite-fayalite solid-solution series (Dyar et al. 2009; Isaacson et al. 2014; Lane et al. 2011). The results from this study expand on previous work by providing critical data for Mg-rich compositions within the Fo_{90}-Fo_{100} range, where Fe-in-olivine absorptions begin to appear in reflectance spectra. These results demonstrate that an absorption feature at ~1 µm can be detected in olivine with 0.01 wt% FeO ($Fo_{99.99}$) under ideal laboratory conditions.

Iron present on the surface of Mercury

The surface of Mercury was thoroughly examined by geochemical instruments onboard NASA's MESSENGER spacecraft (Solomon et al. 2001). When compared to other rocky planetary bodies in our solar system, the surface of Mercury has a high abundance of S (up to 4 wt%) and a low abundance of Fe (~2 wt%), both indicative of planetary processes taking place under highly reduced conditions (e.g., ~3 to 7 log units below the iron-wüstite buffer) (Evans et al. 2012; Malavergne et al. 2010; McCubbin et al. 2012, 2017; Namur et al. 2016; Nittler et al. 2011; Weider et al. 2012, 2014; Zolotov et al. 2011, 2013). Vander Kaaden et al. (2017) used the geochemical data obtained from MESSENGER's X-ray spectrometer (XRS) and Gamma-Ray Spectrometer to calculate the normative mineralogy on the surface of Mercury using a variation on the CIPW norm calculation to include exotic sulfide minerals like niningerite (MgS) and oldhamite (CaS). These calculations, as well as high-temperature and high-pressure experiments, indicated that the silicate mineralogy on the surface of Mercury likely includes plagioclase, Mg-rich pyroxene, Mg-rich olivine, and minor quartz (Namur and Charlier 2017; Vander Kaaden et al. 2017). Given the ~2 wt% Fe measured on the surface, initial interpretations of the MESSENGER data suggested that this iron was present as FeO in silicate minerals (Nittler et al. 2011; Weider et al. 2012), although at least some is also likely from exogenous sources that arrived as reduced Fe^0.

The results of the present study show that 0.01 wt% FeO in olivine produces a detectable 1 µm absorption band in the VIS-NIR spectral range and that FeO variations in olivine from 0.37 to <0.05 wt% can be distinguished in the MIR under ideal laboratory conditions. If the iron measured by MESSENGER instruments is present in relatively young, unweathered silicate minerals on the surface of Mercury, a definitive 1 µm absorption band would be expected in the UV-VIS-NIR data. Izenberg et al. (2014) determined an average spectrum for the surface of Mercury with the data obtained from the Mercury Atmospheric and Surface Composition Spectrometer (MASCS). An average

Table 4. Summary of spectral band parameters calculated for low FeO olivine

	F-S-003 (Mg# 99.99)	F-S-007 (Mg# 99.99)	F-S-006 (Mg# 99.97)	F-S-002 (Mg# 99.95)	F-T-004 (Mg# 99.64)	F-T-002 (Mg# 99.62)	SC001 (Mg# 90.91)	Average (Mg# 99.62–99.64)	Average (Mg# 99.95–99.99)
RELAB ID	OL-RLK-024	OL-RLK-027	OL-RLK-026	OL-RLK-023	OL-RLK-022	OL-RLK-021	OL-RLK-028		
FeO (wt%)	0.01	0.01	0.03	0.05	0.37	0.39	9.01	0.38	0.025
Mg#	99.99	99.99	99.97	99.95	99.64	99.62	90.91	99.63	99.975
Ultraviolet (UV) Region (wavelength nm)									
BC (495 nm)	500	470	500	460	480	470	455	475	482.5
BD (495 nm)	0.0023	0.0032	0.0028	0.0031	0.0962	0.0048	0.0310	0.0505	0.0028
Visible - Near Infrared (VIS-NIR) Region (wavelength μm)									
BC (1.0 μm)	1.08	1.05	1.05	1.06	1.06	1.06	1.06	1.06	1.06
BD (1.0 μm)	0.0069	0.0096	0.0173	0.0305	0.0695	0.0715	0.5151	0.0705	0.0161
IMIR Region (wavelength μm)									
BC (4.9 μm)	4.92	4.92	4.92	4.92	4.92	4.92	4.95	4.92	4.92
BC (5.2 μm)	5.20	5.20	5.20	5.20	5.20	5.20	5.23	5.20	5.20
BC (5.4 μm)	5.44	5.44	5.44	5.44	5.44	5.44	5.46	5.44	5.44
BC (5.6 μm)	5.61	5.61	5.61	5.61	5.61	5.61	5.62	5.61	5.61
BC (6.0 μm)	5.99	5.99	5.98	5.98	5.98	5.99	5.99	5.98	5.98
Mid-Infrared Region (wavenumber cm^{-1})									
CF1	1139.75	1145.53	1147.46	1157.10	1126.25	1124.32	1122.39	1125.29	1147.46
CF2	673.05	669.19	669.19	674.98	673.05	653.76	665.34	663.41	671.60
1	1070.32	1072.25	1072.25	1072.25	1076.11	1078.04	1068.40	1077.08	1071.77
2	991.26	993.18	991.26	989.33	991.26	991.26	985.47	991.26	991.26
3	950.76	950.76	950.76	954.61	946.90	948.83	946.90	947.86	951.72
4	836.97		836.97	838.90	836.97			836.97	837.62
5	622.91	624.84	632.55	632.55	632.55	624.84	634.48	628.69	628.21
6	532.27	530.34	530.34	532.27	528.41	530.34	528.41	529.37	531.30
7	507.20	507.20	507.20	509.12	507.20	507.20	503.34	507.20	507.68
8	476.34	476.34	476.34	476.34	474.41	474.41	468.62	474.41	476.34
9	420.41	420.41	420.41	422.34	420.41	420.41	418.48	420.41	420.90
10	403.06	403.06	403.06	403.06	403.06	403.06	399.20	403.06	403.06
11	362.56	362.56	362.56	364.49	362.56	360.63	356.77	361.59	363.04
12	333.63	333.63	335.56		335.56	331.70	331.70	333.63	334.27
13	293.13	293.13	293.13	293.13	293.13	293.13	287.35	293.13	293.13

spectrum was derived from more than 850 000 spectra acquired across the planet, covering several terranes with different surface ages, and yet this data showed no evidence of a 1 μm absorption band within noise. Murchie et al. (2015) also analyzed a global multispectral map of Mercury acquired by the Mercury Dual Imaging System (MDIS) onboard MESSENGER. Similarly, they found no definitive absorptions that could be attributed to Fe^{2+} in silicates or sulfides, confirming the results from MASCS. In addition to the lack of a 1 μm absorption band, the observed average spectral data have a low (dark) absolute reflectance that ranges between ~0.03 and 0.15 from UV/VIS to NIR, as well as a positive (reddening) slope (Izenberg et al. 2014). These features are consistent with the presence of either macroscopic Fe metal (Cloutis et al. 2015; Matsumoto et al. 2020) or nano-phase Fe (npFe) that forms as a result of space weathering (Allen et al. 1993). The spectral characteristics of the various terranes on the surface of Mercury, in combination with the results from this study, suggest that the Fe present on the surface measured by the XRS on MESSENGER is not present as structural Fe^{2+} within olivine grains.

To quantify detectability from orbital spectrometers that have significantly more noise contributing to the signal, one can estimate the required noise level where the 1 μm band depth is not less than ~5 times the typical noise (Izenberg et al. 2014). The detectability of $Fo_{99.99}$, $Fo_{99.62}$, and $Fo_{90.91}$ would require noise level <0.003, 0.018, and 0.247 (SNR of 320, 41, and 2), respectively. With the MESSENGER VIRS spectrum measured by the MASCS spectrometer having an average noise of 0.012 around the 1 μm wavelength (Izenberg et al. 2014), the present study suggests pure olivine would have been detected at an Mg# <99.62 (0.38 wt% FeO). In other words, taking into account MESSENGER MASCS spectrometer signal-to-noise, MESSENGER's lack of a 1 μm absorption suggests there is <0.38 wt% FeO on the surface. However, this calculation assumes that a MASCS footprint included only olivine, and Vander Kaaden et al. (2017)'s normative mineralogy calculations estimated a maximum of 34.59 wt% olivine in the high-Mg terrane of Mercury. As shown in Figure 8, laboratory and Mercury terrane data resampled to higher spatial resolution, lower noise, but limited spectral resolution MESSENGER MDIS WAC, confirm these detection limits would be discernable in the MDIS spectra, but that the MASCS VIRS data are noise limited. Thus, while the results of this study provide initial constraints for identifying Fe-bearing olivine on the surface of Mercury, improved olivine detection limits will require multiphase laboratory measurements to assess the nonlinearity of multi-component reflectance spectra as well as minimizing noise from orbital spectrometers (Morlok et al. 2023).

Three possible explanations are proposed for the weight percent levels of Fe measured on the surface and concomitant lack of a definitive 1 μm absorption band on Mercury that support surface Fe as a sulfide or metal rather than included in silicates: (1) sulfidization of silicates (Renggli et al. 2022, 2023); (2) graphite-smelting, which would produce macroscopic Fe metal (e.g., Singletary and Grove 2006); and/or (3) space weathering, which would produce nano-phase Fe metal (e.g., Britt and Pieters 1994; Keller and McKay 1997). Iron could be present as troilite produced through the sulfidization of silicate glasses and minerals such as olivine or clinopyroxene (Renggli et al. 2022, 2023). Troilite does not have a 1 μm feature, meaning

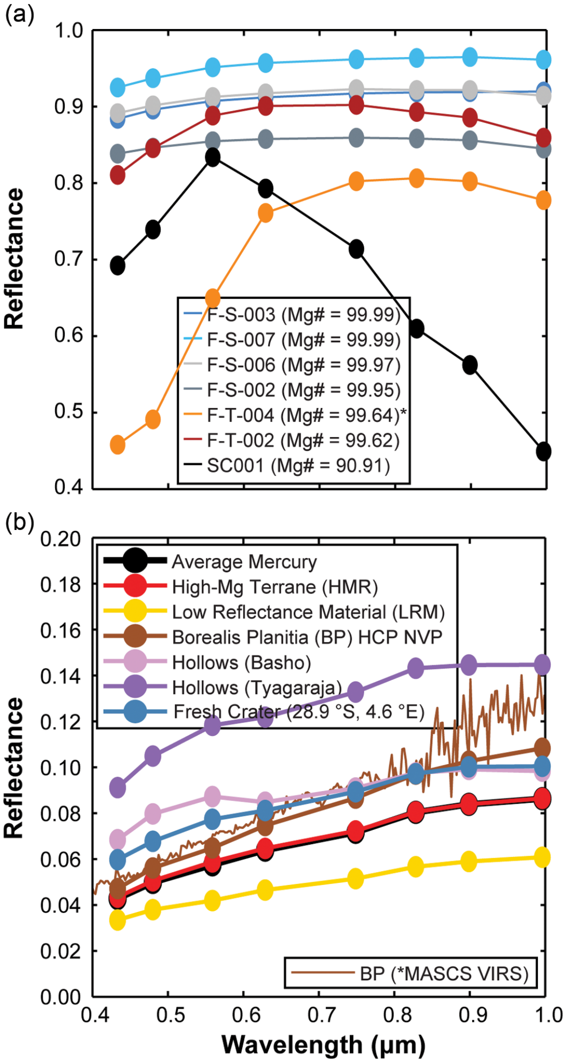

Figure 8. (**a**) Laboratory VIS-NIR reflectance spectra of synthetic olivine powders sieved to <125 μm grain size with median grain sizes from 7.6–54.7 resampled to MESSENGER MDIS WAC filter responses. (**b**) MESSENGER orbital VIS-NIR reflectance spectra of Mercury terranes, including average Mercury and the High-Mg Terrane as well as Low Reflectance Material, Borealis Planitia (HCP NVP), Hollows (Basho), Hollows (Tyagaraja), and a Fresh Crater (data from Murchie et al. 2015). MESSENGER MASCS spectra of Borealis Planitia (HCP NVP) are also shown as measured by MESSENGER MASCS VIRS corrected to 45° incidence angle, 45° emergence angle, 90° phase angle, and in the same reference area as the corresponding MDIS spectra.

current MESSENGER spectra cannot rule it out and would be consistent with wt% levels of both Fe and S on the surface of Mercury (Renggli et al. 2022, 2023). On the basis of the low O/Si ratio measured by the MESSENGER GRS and calculated oxygen deficit on the surface of Mercury, McCubbin et al. (2017) proposed a mechanism whereby elements that are typically oxygen bonded, such as Si and Fe, would be present on the surface of the planet in the form of metals (e.g., Si^0 and Fe^0) due to a smelting process involving the interaction of silicate melt and a globally distributed graphite layer at depth (Vander Kaaden and McCubbin 2015; Peplowski et al. 2016). This smelting process occurs due to the interaction of graphite in Mercury's crust and regolith with FeO-bearing boninitic and komatiitic parental liquids that ascend from depth and erupt onto the surface of Mercury (Klima et al. 2018; Lark et al. 2023; McCubbin et al. 2017; Murchie et al. 2015; Peplowski et al. 2015, 2016; Vander Kaaden and McCubbin 2015, 2016; Xu et al. 2024). The reduction of FeO in the silicate melt to Fe^0 occurs either during ascent or after eruption, leaving behind all Fe in a macroscopic metallic phase that UV-VIS-NIR data cannot detect. The presence of a hypothesized primary graphite crust at the base of the secondary volcanic crust on Mercury would result in most mantle melts coming into contact with graphite during their ascent to the surface. Experimental evidence indicates that graphite is an efficient catalyst for FeO reduction in silicate melts at low pressure (Singletary and Grove 2006; Iacovino et al. 2023), so this process could have been an efficient mechanism for reducing FeO, provided the graphite is globally distributed.

In addition to smelting, space weathering processes have also been shown to produce Fe-metal but in the form of npFe (Pieters and Noble 2016; Noble et al. 2007; Britt and Pieters 1994; Keller and McKay 1997), and this process has also been proposed as a potential explanation for the low O/Si ratio measured by the MESSENGER GRS (McCubbin et al. 2017). Specifically, space weathering processes reduce the structural Fe^{2+} present in ferromagnesian phases to npFe (Britt and Pieters 1994; Keller and McKay 1997). The presence of npFe produced during space weathering can eliminate the characteristic 1 μm absorption band in ferromagnesian silicates in samples with up to 4 wt% FeO (Allen et al. 1993). The space weathering environment on Mercury is expected to be intense compared to other rocky bodies in our solar system (Domingue et al. 2014; Hapke 2001; Lucey and Riner 2011; Noble and Pieters 2003; Pieters and Noble 2016; Riner and Lucey 2012), which further supports this mechanism as a contributor to the lack of an observed 1 μm absorption band on Mercury. Given the nature of these two explanations, we infer that the majority of iron measured on the surface by MESSENGER is present in the form of Fe-rich metal.

IMPLICATIONS

This spectral library of extremely low-Fe olivines enables better detection limits of olivine and chemistry on planetary surfaces, including Mercury, E-type asteroids, and the lunar highlands (Burbine et al. 2002; Lucey 1998; Riner et al. 2012). Here, laboratory spectra are compared to NASA MESSENGER MDIS and MASCS VIS-NIR spectra; the results support the conclusion that Fe in the form of metal or sulfide rather than olivine is present on the mercurian surface. However, these laboratory spectra can be soon compared to ESA/JAXA's BepiColombo's Mercury Radiometer and Thermal Infrared Imaging Spectrometer (MERTIS) that will map emissivity from 7–14 μm at a spectral resolution of 90 nm with a spatial resolution of 500 m/pixel (Hiesinger and Helbert 2010) and also to the visible-near infrared imaging spectrometer (VIHI) of the Spectrometer and Imagers for Mercury Planetary Orbiter

BepiColombo–Integrated Observatory SYStem (SIMBIO-SYS), which will map reflectance from 0.4–2 μm at a spectral resolution of 6.25 nm with a spatial resolution of 100–375 m/pixel (Flamini et al. 2010). ESA/JAXA's BepiColombo mission is exciting because it will measure the MIR spectra of Mercury from orbit for the first time and cover most of Mercury's surface, including the north polar regions and the southern hemisphere (where MESSENGER focused on the northern hemisphere due to the spacecraft's highly elliptical orbit). In particular, MERTIS data in conjunction with MIR data in this study (Fig. 8) should allow mineralogical detection of olivine regardless of Mg# and place additional constraints on how Fe and Mg are hosted on Mercury's surface.

Iron-bearing silicates on Mercury, E-type asteroids, and the lunar surface include pyroxene in addition to olivine (Burbine et al. 2002; Clark et al. 2004; Namur and Charlier 2017; Shearer et al. 2015; Vander Kaaden et al. 2017), and thus a similar effort to synthesize and characterize low FeO pyroxenes over a range of CaO concentrations would provide invaluable insights into the nature and distribution of FeO on low-FeO planetary surfaces. In fact, Fe-free ortho- and clinoenstatites have already been synthesized and characterized for this purpose (e.g., Markus et al. 2018). Procedures for pyroxene synthesis are known (Turnock et al. 1973; Klima et al. 2007; Markus et al. 2018; Lindsley et al. 2019), and the methods employed in the present study can be used to modify established pyroxene synthesis procedures to produce and spectrally characterize similarly Fe-poor pyroxenes.

ACKNOWLEDGMENTS AND FUNDING

Support for this research was provided in part by NASA's Solar System Workings Program (NNX16AL90G). NASA's Planetary Science Division Research Program also supported this research through the ISFM work package Process Simulation and the Jacobs JETS-II contract at Johnson Space Center. This research utilizes spectra acquired by R.L.K. with the NASA RELAB facility at Brown University. The authors thank Justin Reppart for his support in the laboratory. We are thankful for the reviews from Chris Renggli and the anonymous reviewer who strengthened the paper. The forsteritic olivine samples synthesized in this study will be curated at NASA JSC and made available upon request to future investigators for further characterization.

REFERENCES CITED

Adams, J.B. (1975) Interpretation of visible and near-infrared diffuse reflectance spectra of pyroxenes and other rock forming minerals. In C. Karr Jr., Ed., Infrared and Raman Spectroscopy of Lunar and Terrestrial Minerals, p. 91–116. Academic Press.

Agresti, D.G. and Gerakines, P.A. (2009) Simultaneous fitting of Mars Mössbauer data. Hyperfine Interactions, 188, 113–120, https://doi.org/10.1007/s10751-008-9896-1.

Agresti, D.G., Dyar, M.D., and Schaefer, M.W. (2006) Velocity scales for Mars Mössbauer data. Hyperfine Interactions, 170, 67–74, https://doi.org/10.1007/s10751-006-9472-5.

Allen, C.C., Morris, R.V., Lauer, H.V. Jr., and McKay, D.S. (1993) microscopic iron metal on glass and minerals—A tool for studying regolith maturity. Icarus, 104, 291–300, https://doi.org/10.1006/icar.1993.1102.

Britt, D.T. and Pieters, C.M. (1994) Darkening in black and gas-rich ordinary chondrites: The spectral effects of opaque morphology and distribution. Geochimica et Cosmochimica Acta, 58, 3905–3919, https://doi.org/10.1016/0016-7037(94)90370-0.

Burbine, T.H., McCoy, T.J., Nittler, L.R., Benedix, G.K., Cloutis, E.A., and Dickinson, T.L. (2002) Spectra of extremely reduced assemblages: Implications for Mercury. Meteoritics & Planetary Science, 37, 1233–1244, https://doi.org/10.1111/j.1945-5100.2002.tb00892.x.

Burns, R.G. (1970) Crystal field spectra and evidence of cation ordering in olivine minerals. American Mineralogist, 55, 1608–1632.

Burns, R.G. (1993) Mineralogical Applications of Crystal Field Theory, 2nd Edition, 576 p. Cambridge University Press.

Clark, B.E., Bus, S.J., Rivkin, A.S., McConnochie, T., Sanders, J., Shah, S., Hiroi, T., and Shepard, M. (2004) E-type asteroid spectroscopy and compositional modeling. Journal of Geophysical Research: Planets, 109(E2).

Clark, R.N. (1999) Chapter 1: Spectroscopy of Rocks and Minerals, and Principles of Spectroscopy. In A.N. Rencz, Ed., Manual of Remote Sensing, Volume 3, Remote Sensing for the Earth Sciences, p. 3–58. Wiley.

Cloutis, E.A., Sanchez, J.A., Reddy, V., Gaffey, M.J., Binzel, R.P., Burbine, T.H., Hardersen, P.S., Hiroi, T., Lucey, P.G., Sunshine, J.M., and others. (2015) Olivine-metal mixtures: Spectral reflectance properties and application to asteroid reflectance spectra. Icarus, 252, 39–82, https://doi.org/10.1016/j.icarus.2014.10.003.

Day, J.M.D., Corder, C.A., Assayag, N., and Cartigny, P. (2019) Ferrous oxide-rich asteroid achondrites. Geochimica et Cosmochimica Acta, 266, 544–567, https://doi.org/10.1016/j.gca.2019.04.005.

Domingue, D.L., Chapman, C.R., Killen, R.M., Zurbuchen, T.H., Gilbert, J.A., Sarantos, M., Benna, M., Slavin, J.A., Schriver, D., Travnicek, P.M., and others. (2014) Mercury's weather-beaten surface: Understanding Mercury in the context of lunar and asteroidal space weathering studies. Space Science Reviews, 181, 121–214, https://doi.org/10.1007/s11214-014-0039-5.

Dyar, M.D., Sklute, E.C., Menzies, O.N., Bland, P.A., Lindsley, D., Glotch, T., Lane, M.D., Schaefer, M.W., Wopenka, B., Klima, R., and others. (2009) Spectroscopic characteristics of synthetic olivine: An integrated multi-wavelength and multi-technique approach. American Mineralogist, 94, 883–898, https://doi.org/10.2138/am.2009.3115.

Evans, L.G., Peplowski, P.N., Rhodes, E.A., Lawrence, D.J., McCoy, T.J., Nittler, L.R., Solomon, S.C., Sprague, A.L., Stockstill-Cahill, K.R., Starr, R.D., and others. (2012) Major-element abundances on the surface of Mercury: Results from the MESSENGER Gamma-Ray Spectrometer. Journal of Geophysical Research. Planets, 117, E00L07.

Filiberto, J. and Dasgupta, R. (2011) Fe^{2+}-Mg partitioning between olivine and basaltic melts: Applications to genesis of olivine-phyric shergottites and conditions of melting in the Martian interior. Earth and Planetary Science Letters, 304, 527–537, https://doi.org/10.1016/j.epsl.2011.02.029.

Flamini, E., Capaccioni, F., Colangeli, L., Cremonese, G., Doressoundiram, A., Josset, J.L., Langevin, Y., Debei, S., Capria, M.T., De Sanctis, M.C., and others. (2010) SIMBIO-SYS: The spectrometer and imagers integrated observatory system for the BepiColombo planetary orbiter. Planetary and Space Science, 58, 125–143, https://doi.org/10.1016/j.pss.2009.06.017.

Fournelle, J.H. (2011) An investigation of "San Carlos Olivine": Comparing USNM-distributed material with commercially available material. Microscopy and Microanalysis, 17, 842–843, https://doi.org/10.1017/S1431927611005083.

Hamilton, V.E. (2010) Thermal infrared (vibrational) spectroscopy of Mg-Fe olivines: A review and applications to determining the composition of planetary surfaces. Chemie der Erde, 70, 7–33, https://doi.org/10.1016/j.chemer.2009.12.005.

Hapke, B. (2001) Space weathering from Mercury to the asteroid belt. Journal of Geophysical Research: Solid Earth, 106, 10039–10073, https://doi.org/10.1029/2000JE001338.

Hiesinger, H. and Helbert, J. (2010) The Mercury radiometer and thermal infrared spectrometer (MERTIS) for the BepiColombo mission. Planetary and Space Science, 58, 144–165, https://doi.org/10.1016/j.pss.2008.09.019.

Holsclaw, G.M., McClintock, W.E., Domingue, D.L., Izenberg, N.R., Blewett, D.T., and Sprague, A.L. (2010) A comparison of the ultraviolet to near-infrared spectral properties of Mercury and the Moon as observed by MESSENGER. Icarus, 209, 179–194, https://doi.org/10.1016/j.icarus.2010.05.001.

Iacovino, K., McCubbin, F.M., Vander Kaaden, K.E., Clark, J., Wittmann, A., Jakubek, R.S., Moore, G.M., Fries, M.D., Archer, D., and Boyce, J.W. (2023) Carbon as a key driver of super-reduced explosive volcanism on Mercury: Evidence from graphite-melt smelting experiments. Earth and Planetary Science Letters, 602, 117908, https://doi.org/10.1016/j.epsl.2022.117908.

Isaacson, P., Klima, R., Sunshine, J., Cheek, L., Pieters, C.M., Hiroi, T., Dyar, M.D., Lane, M., and Bishop, J. (2014) Visible to near-infrared optical properties of pure synthetic olivine across the olivine solid solution. American Mineralogist, 99, 467–478, https://doi.org/10.2138/am.2014.4580.

Izenberg, N.R., Klima, R.L., Murchie, S.L., Blewett, D.T., Holsclaw, G.M., McClintock, W.E., Malaret, E., Mauceri, C., Vilas, F., Sprague, A.L., and others. (2014) The low-iron, reduced surface of Mercury as seen in spectral reflectance by MESSENGER. Icarus, 228, 364–374, https://doi.org/10.1016/j.icarus.2013.10.023.

Jackson, C.R., Cheek, L.C., Williams, K.B., Hanna, K.D., Pieters, C.M., Parman, S.W., Cooper, R.F., Dyar, M.D., Nelms, M., and Salvatore, M.R. (2014) Visible-infrared spectral properties of iron-bearing aluminate spinel under lunar-like redox conditions. American Mineralogist, 99, 1821–1833, https://doi.org/10.2138/am-2014-4793.

Karner, J., Papike, J.J., and Shearer, C.K. (2003) Olivine from planetary basalts: Chemical signatures that indicate planetary parentage and those that record igneous setting and process. American Mineralogist, 88, 806–816, https://doi.org/10.2138/am-2003-5-609.

Keller, L.P. and McKay, D.S. (1997) The nature and origin of rims on lunar soil grains. Geochimica et Cosmochimica Acta, 61, 2331–2341, https://doi.org/10.1016/S0016-7037(97)00085-9.

King, T.V.V. and Ridley, W.I. (1987) Relation of the spectroscopic reflectance of olivine to mineral chemistry and some remote sensing implications. Journal of Geophysical Research, 92, 11457–11469.

Klima, R.L., Pieters, C.M., and Dyar, M.D. (2007) Spectroscopy of synthetic Mg-Fe pyroxenes I: Spin-allowed and spin-forbidden crystal field bands in the visible and near-infrared. Meteoritics & Planetary Science, 42, 235–253, https://doi.org/10.1111/j.1945-5100.2007.tb00230.x.

Klima, R.L., Dyar, M.D., and Pieters, C.M. (2011) Near-infrared spectra of clinopyroxenes: Effects of calcium content and crystal structure. Meteoritics & Planetary Science, 46, 379–395, https://doi.org/10.1111/j.1945-5100.2010.01158.x.

Klima, R.L., Denevi, B.W., Ernst, C.M., Murchie, S.L., and Peplowski, P.N. (2018) Global distribution and spectral properties of low-reflectance material on Mercury. Geophysical Research Letters, 45, 2945–2953, https://doi.org/10.1002/2018GL077544.

Klingelhöfer, G., Morris, R.V., Bernhardt, B., Rodionov, D., de Souza, P.A. Jr., Squyres, S.W., Foh, J., Kankeleit, E., Bonnes, U., Gellert, R., and others. (2003) Athena MIMOS II Mössbauer spectrometer investigation. Journal of Geophysical Research: Solid Earth, 108, 8067, https://doi.org/10.1029/2003JE002138.

Kremer, C.H., Mustard, J.F., and Pieters, C.M. (2020) Cross over infrared spectroscopy: A new tool for the remote determination of olivine composition. Geophysical Research Letters, 47, 20, https://doi.org/10.1029/2020GL089151.

Lane, M.D., Glotch, T.D., Dyar, M.D., Pieters, C.M., Klima, R.L., Hiroi, T., Bishop, J.L., and Sunshine, J.M. (2011) Midinfrared spectroscopy of synthetic olivines: Thermal emission, specular and diffuse reflectance, and attenuated total reflectance studies of forsterite to fayalite. Journal of Geophysical Research: Solid Earth, 116, E08010, https://doi.org/10.1029/2010JE003588.

Lark, L.H., Head, J.W., and Huber, C. (2023) Evidence for a carbon-rich Mercury from the distribution of low-reflectance material (LRM) associated with large impact basins. Earth and Planetary Science Letters, 613, 118192, https://doi.org/10.1016/j.epsl.2023.118192.

Lindsley, D.H., Nekvasil, H., and Glotch, T.D. (2019) Synthesis of pigeonites for spectroscopic studies. American Mineralogist, 104, 615–618, https://doi.org/10.2138/am-2019-6869CCBYNCND.

Longhi, J., Durand, S.R., and Walker, D. (2010) The pattern of Ni and Co abundances in lunar olivines. Geochimica et Cosmochimica Acta, 74, 784–798, https://doi.org/10.1016/j.gca.2009.10.001.

Lucey, P. (1998) Model near-infrared optical constants of olivine and pyroxene as a function of iron content. Journal of Geophysical Research: Planets, 103.E1, 1703–1713.

Lucey, P.G. and Riner, M.A. (2011) The optical effects of small iron particles that darken but do not redden: Evidence of intense space weathering on Mercury. Icarus, 212, 451–462, https://doi.org/10.1016/j.icarus.2011.01.022.

Malavergne, V., Toplis, M.J., Berthet, S., and Jones, J. (2010) Highly reducing conditions during core formation on Mercury: Implications for internal structure and the origin of a magnetic field. Icarus, 206, 199–209, https://doi.org/10.1016/j.icarus.2009.09.001.

Markus, K., Moroz, L., Arnold, G., Henckel, D., Hiesinger, H., Rohrbach, A. and Klemme, S. (2018) Reflectance spectra of synthetic Fe-free ortho- and clinoenstatites in the UV/VIS/IR and implications for remote sensing detection of Fe-free pyroxenes on planetary surfaces. Planetary and Space Science, 159, 43–55.

Matsumoto, T., Harries, D., Langenhorst, F., Miyake, A., and Noguchi, T. (2020) Iron whiskers on asteroid Itokawa indicate sulfide destruction by space weathering. Nature Communications, 11, 1117, https://doi.org/10.1038/s41467-020-14758-3.

McCubbin, F.M., Riner, M.A., Vander Kaaden, K.E., and Burkemper, L.K. (2012) Is Mercury a volatile-rich planet? Geophysical Research Letters, 39, L09202.

McCubbin, F.M., Vander Kaaden, K.E., Peplowski, P.N., Bell, A.S., Nittler, L.R., Boyce, J.W., Evans, L.G., Keller, L.P., Elardo, S.M., and McCoy, T.J. (2017) A low O/Si ratio on the surface of Mercury: Evidence for silicon smelting? Journal of Geophysical Research. Planets, 122, 2053–2076, https://doi.org/10.1002/2017JE005367.

Morlok, A., Renggli, C., Charlier, B., Namur, O., Klemme, S., Reitze, M.P., Weber, I., Stojic, A.N., Bauch, K.E., Hiesinger, H., and others. (2023) A mid-infrared study of synthetic glass and crystal mixtures analog to the geochemical terranes on mercury. Icarus, 396, 115498, https://doi.org/10.1016/j.icarus.2023.115498.

Morris, R.V., Klingelhöfer, G., Schröder, C., Rodionov, D.S., Yen, A., Ming, D.W., De Souza, P.A. Jr., Fleischer, I., Wdowiak, T., Gellert, R., and others. (2006) Mössbauer mineralogy of rock, soil, and dust at Gusev Crater, Mars: Spirit's journey through weakly altered olivine basalt on the Plains and pervasively altered basalt in the Columbia Hills. Journal of Geophysical Research: Solid Earth, 111, E02S13, https://doi.org/10.1029/2005JE002584.

Murchie, S.L., Klima, R.L., Denevi, B.W., Ernst, C.M., Keller, M.R., Domingue, D.L., Blewett, D.T., Chabot, N.L., Hash, C., Malaret, E., and others. (2015) Orbital multispectral mapping of Mercury with the MESSENGER Mercury Dual Imaging System: Evidence for the origins of plains units and low-reflectance material. Icarus, 254, 287–305, https://doi.org/10.1016/j.icarus.2015.03.027.

Namur, O. and Charlier, B. (2017) Silicate mineralogy at the surface of Mercury. Nature Geoscience, 10, 9–13, https://doi.org/10.1038/ngeo2860.

Namur, O., Charlier, B., Holtz, F., Cartier, C., and McCammon, C. (2016) Sulfur solubility in reduced mafic silicate melts: Implications for the speciation and distribution of sulfur on Mercury. Earth and Planetary Science Letters, 448, 102–114, https://doi.org/10.1016/j.epsl.2016.05.024.

Nittler, L.R., Starr, R.D., Weider, S.Z., McCoy, T.J., Boynton, W.V., Ebel, D.S., Ernst, C.M., Evans, L.G., Goldsten, J.O., Hamara, D.K., and others. (2011) The major-element composition of Mercury's surface from MESSENGER X-ray spectrometry. Science, 333, 1847–1850, https://doi.org/10.1126/science.1211567.

Noble, S.K. and Pieters, C.M. (2003) Space weathering on Mercury: Implications for remote sensing. Solar System Research, 37, 31–35, https://doi.org/10.1023/A:1022395605024.

Noble, S.K., Pieters, C.M., and Keller, L.P. (2007) An experimental approach to understanding the optical effects of space weathering. Icarus, 192, 629–642, https://doi.org/10.1016/j.icarus.2007.07.021.

Papike, J.J., Karner, J.M., and Shearer, C.K. (2003) Determination of planetary basalt parentage: A simple technique using the electron microprobe. American Mineralogist, 88, 469–472, https://doi.org/10.2138/am-2003-2-323.

Peplowski, P.N., Lawrence, D.J., Evans, L.G., Klima, R.L., Blewett, D.T., Goldsten, J.O., Murchie, S.L., McCoy, T.J., Nittler, L.R., Solomon, S.C., and others. (2015) Constraints on the abundance of carbon in near-surface materials on Mercury: Results from the MESSENGER Gamma-Ray Spectrometer. Planetary and Space Science, 108, 98–107, https://doi.org/10.1016/j.pss.2015.01.008.

Peplowski, P.N., Klima, R.L., Lawrence, D.J., Ernst, C.M., Denevi, B.W., Frank, E.A., Goldsten, J.O., Murchie, S.L., Nittler, L.R., and Solomon, S.C. (2016) Remote sensing evidence for an ancient carbon-bearing crust on Mercury. Nature Geoscience, 9, 273–276, https://doi.org/10.1038/ngeo2669.

Pieters, C.M. (1983) Strength of mineral absorption features in the transmitted component of near-infrared reflected light: First results from RELAB. Journal of Geophysical Research: Solid Earth, 88.B11, 9534–9544.

Pieters, C.M. and Noble, S.K. (2016) Space weathering on airless bodies. Journal of Geophysical Research. Planets, 121, 1865–1884, https://doi.org/10.1002/2016JE005128.

Renggli, C.J., Klemme, S., Morlok, A., Berndt, J., Weber, I., Hiesinger, H., and King, P.L. (2022) Sulfides and hollows formed on Mercury's surface by reactions with reducing S-rich gases. Earth and Planetary Science Letters, 593, 117647, https://doi.org/10.1016/j.epsl.2022.117647.

Renggli, C.J., Stojic, A.N., Morlok, A., Berndt, J., Weber, I., Klemme, S., and Hiesinger, H. (2023) Mid Infrared Spectroscopy of Sulfidation Reaction Products and Implications for Sulfur on Mercury. Journal of Geophysical Research. Planets, 128, e2023JE007895, https://doi.org/10.1029/2023JE007895.

Riner, M.A. and Lucey, P.G. (2012) Spectral effects of space weathering on Mercury: The role of composition and environment. Geophysical Research Letters, 39, L12201, https://doi.org/10.1029/2012GL052065.

Roeder, P.L. and Emslie, R.F. (1970) Olivine-liquid equilibrium. Contributions to Mineralogy and Petrology, 29, 275–289, https://doi.org/10.1007/BF00371276.

Salisbury, J.W. (1993) Mid-infrared spectroscopy: Laboratory data. Remote Geochemical Analysis: Elemental and mineralogical composition 4, 79–98.

Shearer, C.K., Burger, P.V., Papdce, J.J., Borg, L.E., Irving, A.J., and Herd, C. (2008) Petrogenetic linkages among Martian basalts: Implications based on trace element chemistry of olivine. Meteoritics & Planetary Science, 43, 1241–1258, https://doi.org/10.1111/j.1945-5100.2008.tb01126.x.

Shearer, C.K., Elardo, S.M., Petro, N.E., Borg, L.E., and McCubbin, F.M. (2015) Origin of the lunar highlands Mg-suite: An integrated petrology, geochemistry, chronology, and remote sensing perspective. American Mineralogist, 100, 294–325, https://doi.org/10.2138/am-2015-4817.

Shestopalov, D., and Golubeva, L. (2006) *Proceedings of the 37th Lunar and Planetary Science Conference*, p. 1227. Lunar and Planetary Institute.

Singletary, S. and Grove, T.L. (2006) Experimental constraints on ureilite petrogenesis. Geochimica et Cosmochimica Acta, 70, 1291–1308, https://doi.org/10.1016/j.gca.2005.10.034.

Solomon, S.C., McNutt, R.L. Jr., Gold, R.E., Acuña, M.H., Baker, D.N., Boynton, W.V., Chapman, C.R., Cheng, A.F., Gloeckler, G., Head, J.W. III, and others. (2001) The MESSENGER mission to Mercury: Scientific objectives and implementation. Planetary and Space Science, 49, 1445–1465, https://doi.org/10.1016/S0032-0633(01)00085-X.

Sunshine, J.M. and Pieters, C.M. (1998) Determining the composition of olivine from reflectance spectroscopy. Journal of Geophysical Research: Solid Earth, 103 (E6), 13675–13688, https://doi.org/10.1029/98JE01217.

Toplis, M.J. (2005) The thermodynamics of iron and magnesium partitioning between olivine and liquid: Criteria for assessing and predicting equilibrium in natural and experimental systems. Contributions to Mineralogy and Petrology, 149, 22–39, https://doi.org/10.1007/s00410-004-0629-4.

Turnock, A.C., Lindsley, D.H. and Grover, J.E. (1973) Synthesis and unit cell parameters of Ca-Mg-Fe pyroxenes. American Mineralogist, 58, 50–59.

Vander Kaaden, K.E. and McCubbin, F.M. (2015) Exotic crust formation on Mercury: Consequences of a shallow, FeO-poor mantle. Journal of Geophysical Research. Planets, 120, 195–209, https://doi.org/10.1002/2014JE004733.

——— (2016) The origin of boninites on Mercury: An experimental study of the northern volcanic plains lavas. Geochimica et Cosmochimica Acta, 173, 246–263, https://doi.org/10.1016/j.gca.2015.10.016.

Vander Kaaden, K.E., Agee, C.B., and McCubbin, F.M. (2015) Density and compressibility of the molten lunar picritic glasses: Implications for the roles of Ti and Fe in the structures of silicate melts. Geochimica et Cosmochimica Acta, 149, 1–20, https://doi.org/10.1016/j.gca.2014.10.029.

Vander Kaaden, K.E., McCubbin, F.M., Nittler, L.R., Peplowski, P.N., Weider, S.Z., Frank, E.A., and McCoy, T.J. (2017) Geochemistry, mineralogy, and petrology of boninitic and komatiitic rocks on the mercurian surface: Insights into the mercurian mantle. Icarus, 285, 155–168, https://doi.org/10.1016/j.icarus.2016.11.041.

Weider, S.Z., Nittler, L.R., Starr, R.D., McCoy, T.J., Stockstill-Cahill, K.R., Byrne, P.K., Denevi, B.W., Head, J.W., and Solomon, S.C. (2012) Chemical heterogeneity on Mercury's surface revealed by the MESSENGER X-ray Spectrometer. Journal of Geophysical Research. Planets, 117, E00L05.

Weider, S.Z., Nittler, L.R., Starr, R.D., McCoy, T.J., and Solomon, S.C. (2014) Variations in the abundance of iron on Mercury's surface from MESSENGER X-ray Spectrometer observations. Icarus, 235, 170–186, https://doi.org/10.1016/j.icarus.2014.03.002.

Williams, K.B., Jackson, C.R., Cheek, L.C., Donaldson-Hanna, K.L., Parman, S.W., Pieters, C.M., Dyar, M.D., and Prissel, T.C. (2016) Reflectance spectroscopy of chromium-bearing spinel with application to recent orbital data from the Moon. American Mineralogist, 101, 726–734, https://doi.org/10.2138/am-2016-5535.

Xu, R., Xiao, Z., Wang, Y., and Cui, J. (2024) Less than one weight percent of graphite on the surface of Mercury. Nature Astronomy, 8, 280–289, https://doi.org/10.1038/s41550-023-02169-5.

Zolotov, M.Y., Sprague, A.L., Nittler, L.R., Weider, S.Z., Starr, R.D., Evans, L.G., Boynton, W.V., Goldstein, J.O., Hauck, S.A., and Solomon, S.C. (2011) Implications of the MESSENGER discovery of high sulfur abundance on the surface of Mercury. *American Geophysical Union Fall Meeting Abtracts*, #1584.

Zolotov, M.Y., Sprague, A.L., Hauck, S.A. II, Nittler, L.R., Solomon, S.C., and Weider, S.Z. (2013) The redox state, FeO content, and origin of sulfur-rich magmas on Mercury. Journal of Geophysical Research. Planets, 118, 138–146, https://doi.org/10.1029/2012JE004274.

Manuscript received March 25, 2024
Manuscript accepted August 15, 2024
Accepted manuscript online August 27, 2024
Manuscript Handled by Heather Watson

Endnotes:

Deposit item AM-25-49400. Online Materials are free to all readers. Go online, via the table of contents or article view, and find the tab or link for supplemental materials.